



Numerical simulation of the failure process of unreinforced masonry walls due to concentrated static and dynamic loading

S.Y. Wang^{a,*}, S.W. Sloan^a, A.J. Abbo^a, M.J. Masia^b, C.A. Tang^c

^a Centre for Geotechnical and Materials Modelling, Civil, Surveying and Environmental Engineering, The University of Newcastle, Callaghan, NSW 2308, Australia

^b Centre for Infrastructure Performance and Reliability, School of Engineering, The University of Newcastle, Callaghan, NSW 2308, Australia

^c School of Civil and Hydraulic Engineering, Dalian University of Technology, Dalian 116024, PR China

ARTICLE INFO

Article history:

Received 6 May 2011

Received in revised form 2 October 2011

Available online 22 October 2011

Keywords:

Masonry

Concentrated loads

Numerical simulation

Cracks

Fracture process

ABSTRACT

Finite element analyses of brick masonry subjected to in-plane concentrated static and dynamic loads are carried out to study crack initiation and propagation during the failure process of unreinforced masonry walls. The numerical model is firstly validated by the experimental tests by using the same materials parameters and loading conditions. Then, the static and dynamic concentrated loads are applied to the mortar joints and brick, respectively, and numerical simulations are used to compare the fracture characteristics for these loads. In addition, a comparison of fracture mechanisms for the concentrated loads on the mortar joint and brick is also given. Finally, the effect of dynamic pressure (P_{\max}) on the failure mechanism of brick masonry is considered.

Crown Copyright © 2011 Published by Elsevier Ltd. All rights reserved.

1. Introduction

Brick masonry is an ancient building technique, and masonry structures constitute a large portion of buildings around the world. Such structures and buildings are sometimes required to withstand exceptional dynamic loading resulting from accidental impact or seismic activity (Mackerle, 2004). In addition, masonry is a composite material made of brick units, which are usually made from clay, and mortar joints. Many variables influence the mechanical behaviour of masonry, such as the brick and mortar properties, brick geometry, joint dimensions, and joint arrangement, which results in heterogeneous masonry material (Cecchi and Rizzi, 2001). However, masonry was often assumed to be isotropic elastic in early analyses (Wood, 1952; Rosenhaupt and Sokoal, 1965; Pande et al., 1989). The development of numerical techniques led to more refined models that model bricks and joints separately and allow for local failure inside three components (Lourenco and Rots, 1997; Ali and Page, 1998).

In terms of model scale, masonry structures can be modelled at the micro-, meso- and macro- levels. For micro- and meso-scale analyses, a detailed representation of bricks and mortar can be given (Rots, 1991). In addition, using a grade of refinement scheme, a structure modelled at the micro-scale or meso-scale could be set

up for macro-scale analysis (Dhanasekar et al., 1985; Lofti and Shing, 1991; Lourenco, 1996; Guinea et al., 2000; Massart et al., 2005; Pina-Henriques and Lourenco, 2006; Shieh-Beygi and Pietruszczak, 2008). Usually, for large structures, an elastic and homogeneous material law is adopted for the masonry composite to predict the deformations and structural displacements at low and medium stress levels, whereas such an approximation is not sufficient to assess masonry failures (Anthoine, 1997; Guinea et al., 2000; Lourenco and Rots, 2000; Bigoni and Piccolroaz, 2004). Because tensile crack initiation and propagation always results from existing micro-defects or fractures in the mortar, brick and mortar/brick interface, the stress redistribution is then directly influenced by the heterogeneity of the material at the meso-scale (Rosenhaupt and Sokoal 1965; Page, 1983; Massart et al., 2005).

Furthermore, strain-rate effects in concrete or brick mortar are induced by high-amplitude short-duration dynamic loads and are thus important in design and analysis. In the past, many laboratory experiments were carried out to investigate the performance of masonry or concrete at high load or strain rate (Ross et al., 1989; Yon et al., 1992; Tedesco et al., 1993; Bažant et al., 1995; Ross et al., 1995; Gilbert et al. 2002). This yields general knowledge about the effects of the strain rate on the strength and fracture characteristics of concrete or masonry. In addition, many numerical analyses using the FEM have been conducted to determine the stress distribution in specimens under different loading conditions (Tedesco et al., 1989, 1991; Mackerle, 2000; Massart et al., 2004; Milani et al. 2009). Essawy et al. (1985) reported a finite element model to track the progress of cracking in a masonry wall.

* Corresponding author.

E-mail addresses: Shanyong.Wang@newcastle.edu.au (S.Y. Wang), Scott.Sloan@newcastle.edu.au (S.W. Sloan), Andrew.Abbo@newcastle.edu.au (A.J. Abbo), Mark.Masia@newcastle.edu.au (M.J. Masia), catang@mechsoft.cn (C.A. Tang).

Burnett et al. (2007) developed a simplified discrete-crack finite element modelling approach to model the performance of unreinforced brickwork and blockwork masonry walls subject to out-of-plane impacts. Furthermore, a particle model consisting in a phenomenological discontinuum approach was proposed by Pina-Henriques and Lourenco (2006) to represent the microstructure of masonry components. Morris et al. (2006) reported the combined finite element/discrete element to investigate the effect of explosive and impact loading on geological media. However, few of the models reported can actually capture the whole fracture process due to dynamic loading of masonry as characterised by initiation, propagation, and coalescence of microcracks. Therefore, the performance of masonry walls subjected to concentrated impact loadings has been poorly understood.

Many structures are built with brittle materials, such as rock, concrete or masonry. It is now accepted that the failure mechanism in brittle materials is controlled by crack initiation, propagation and coalescence (Essawy et al., 1985; Tang and Kou, 1998). From the viewpoint of damage mechanics, the non-linear behaviour of quasi-brittle solids under loading is caused by progressive damage of the microstructure (Ju et al., 1989; Massart et al., 2004). The Realistic Failure Process Analysis (RFPA) Code, developed by Tang (Tang, 1997; Tang et al., 2000), simulates the quasi-static fracture process of rock and concrete using a meso-mechanical model. When a concrete specimen is subjected to a shock or an explosion, the material is subjected to various states of stress that yield different failure modes. Near the impact location severe hydrostatic compression is observed, while farther from the impact location the material experiences compression with a moderate triaxial state of stress. Finally, compressive wave reflection may occur and can result in a tensile wave, which will interact with compressive waves and produce spalling, i.e., tensile cracking induced by wave interaction (Zhu et al., 2004).

The current paper presents a stain-rate-sensitive model for masonry failure based on damage mechanics to simulate the fracture process of brick masonry subjected to static and dynamic (impact) loading. For this numerical model, the brick masonry is assumed to be a three-phase composite composed of brick, mortar joint and interfaces between the brick and mortar joints. A constitutive law, which is based on damage mechanics and considers the effect of strain rate on strength, is proposed (Chau et al., 2004). Both the maximum tensile strain criterion and Mohr-Coulomb criterion are utilised as the damage threshold for mesoscopic elements. The present model allows for nonlinear material characteristics and progressive local cracking. The load is applied incrementally to determine the response of the wall from the first crack through to final failure.

The following section describes the materials used in this work and the tests performed. Section 2 briefly presents the proposed mechanism of this numerical model. Section 3 describes the model setup and the numerically simulated results. Section 4 concludes the paper.

2. Brief description of RFPA^{2D}

Briefly, the code Realistic Failure Process Analysis (RFPA^{2D}) (Tang, 1997) is a two-dimensional finite element code that can simulate the fracture and failure process of quasi-brittle materials, such as rock, concrete and masonry. To model the failure of a brittle material, the medium is assumed to be composed of many mesoscopic rectangular elements of the same size. In the current study, to capture the heterogeneity of masonry at the meso-level, the mechanical properties of each phase, including the elastic modulus, the strength and Poisson's ratio, are all assumed to conform to the Weibull distribution as defined by the following probability density function (Weibull, 1951):

$$f(u) = \frac{m}{u_0} \left(\frac{u}{u_0} \right)^{m-1} \exp \left[- \left(\frac{u}{u_0} \right)^m \right] \quad (1)$$

where u is a given mechanical property (such as the strength or elastic modulus); u_0 is the scale parameter; and m is the shape parameter that defines the shape of the distribution function. In the present study, the parameter m defines the degree of material homogeneity and is thus referred to as the homogeneity index. As the homogeneity index increases, the material becomes more homogeneous. Each of the element material properties are different and are specified according to the Weibull distribution, with four-node iso-parametric elements being used in the finite element analysis. Elastic damage mechanics is used to describe the constitutive law of the meso-scale elements, and the maximum tensile strain criterion and the Mohr-Coulomb criterion are utilised as damage thresholds (Zhu and Tang, 2002). In fact, the introduction of Weibull function of mechanical properties of mesoscopic elements plays a role as a bridge from Meso-scale damage of elements to Macro-scale failure of material (Tang, 1997; Zhu and Tang, 2002). This approach of assigning material properties has been shown to be an effective means of simulating the heterogeneity of rock and concrete. The influence of the homogeneity index (m) of the rock/concrete on the failure modes has been investigated in previous publications (Tang, 1997; Zhu and Tang, 2002; Zhu et al., 2005). In the current study, the effect of the homogeneity index of the brick, mortar and the interface between them on the failure modes of masonry structure is not considered.

2.1. Elastic damage constitutive law

In this model, the damage mechanics approach is employed to model the mechanical behaviour of meso-scale elements. For each element, the material is assumed to be linear elastic, isotropic and damage-free before loading, with its elastic properties defined by the elastic modulus and Poisson's ratio. After the initiation of damage, the elastic modulus of an element degrades monotonically as the damage evolves and is expressed as follows (Zhu et al., 2004):

$$E = (1 - D)E_0 \quad (2)$$

where D represents the damage variable; and E and E_0 are the elastic modulus of the damaged and the undamaged material, respectively.

The constitutive relationship of a mesoscopic element under uniaxial tension is expressed as (Zhu and Tang, 2002; Zhu et al., 2004):

$$D = \begin{cases} 0 & \varepsilon < \varepsilon_{t0} \\ 1 - \frac{f_{tr}}{E_0 \varepsilon} & \varepsilon_{t0} \leq \varepsilon \leq \varepsilon_{tu} \\ 1 & \varepsilon > \varepsilon_{tu} \end{cases} \quad (3)$$

where f_{tr} is the residual tensile strength, which is given as $f_{tr} = \lambda f_{t0} = \lambda E_0 \varepsilon_{t0}$; f_{t0} and λ are the uniaxial tensile strength and residual strength coefficients, respectively; ε_{t0} is the strain at the elastic limit, which can be called the *threshold strain*; and ε_{tu} is the ultimate tensile strain of the element at which the element would be completely damaged. The ultimate tensile strain is defined as $\varepsilon_{tu} = \eta \varepsilon_{t0}$, where η is the *ultimate strain coefficient*. Eq. (3) can be expressed as (Zhu and Tang, 2002; Zhu et al., 2004):

$$D = \begin{cases} 0 & \varepsilon < \varepsilon_{t0} \\ 1 - \frac{\lambda \varepsilon_{t0}}{\varepsilon} & \varepsilon_{t0} \leq \varepsilon \leq \varepsilon_{tu} \\ 1 & \varepsilon > \varepsilon_{tu} \end{cases} \quad (4)$$

In addition, it is assumed that the damage of mesoscopic elements in multiaxial stress conditions is also isotropic and elastic (Tang, 1997). Under multiaxial stress states, the element can still be damaged in the tensile mode when the equivalent major tensile strain $\bar{\varepsilon}$

Table 1

Model parameters (Riddington and Naom, 1994).

Constituent	Property	Value
Brick	Young's modulus, E (MPa)	22000
	Poisson's ratio, ν	0.15
	Compressive strength, (MPa)	61.0
	Tensile strength, (MPa)	10.7
	homogeneity index (m)	3
	parameter to reflect the stress rate effect on strength (A)	4.27
Mortar	Young's modulus, E (MPa)	8888
	Poisson's ratio, ν	0.20
	Compressive strength, (MPa)	14.5
	Tensile strength, (MPa)	1.575
	homogeneity index (m)	3
	parameter to reflect the stress rate effect on strength (A)	1.02
Mortar/brick-mortar interface	Shear strength, (MPa)	1.02
	Tensile strength, (MPa)	0.523
	homogeneity index (m)	3

Table 2

Material parameters for indenter.

Young's modulus, E (MPa)	200 GPa
Compressive strength, (MPa)	1000 MPa
Poisson's ratio, ν	0.25

exceeds the threshold strain ε_{t0} . The equivalent principal strain $\bar{\varepsilon}$ is defined as (Zhu and Tang, 2002; Zhu et al., 2004):

$$\bar{\varepsilon} = \sqrt{\langle \varepsilon_1 \rangle^2 + \langle \varepsilon_2 \rangle^2 + \langle \varepsilon_3 \rangle^2} \quad (5)$$

where ε_1 , ε_2 and ε_3 are three principal strains and $\langle \rangle$ is a function defined as follows:

$$\langle x \rangle = \begin{cases} x & x \geq 0 \\ 0 & x < 0 \end{cases} \quad (6)$$

The constitutive law of an element subjected to multiaxial stresses can be easily obtained by substituting the equivalent strain $\bar{\varepsilon}$ for the strain ε in Eqs. (3) and (4). The damage variable then becomes (Zhu and Tang, 2002; Zhu et al., 2004):

$$D = \begin{cases} 0 & \bar{\varepsilon} < \varepsilon_{t0} \\ 1 - \frac{\lambda \varepsilon_{t0}}{\bar{\varepsilon}} & \varepsilon_{t0} \leq \bar{\varepsilon} \leq \varepsilon_{tu} \\ 1 & \bar{\varepsilon} > \varepsilon_{tu} \end{cases} \quad (7)$$

To simulate the damage of an element when it is under compressive/shear, the Mohr-Coulomb criterion is chosen to be the second damage threshold (Zhu and Tang, 2002; Zhu et al., 2004) according to

$$F = \sigma_1 - \frac{1 + \sin \phi}{1 - \sin \phi} \sigma_3 \geq f_{c0} \quad (8)$$

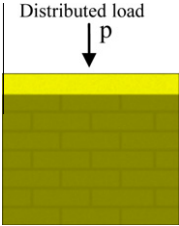
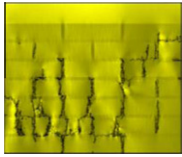
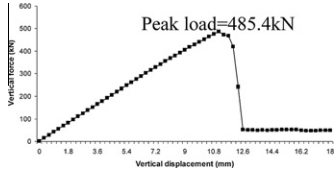
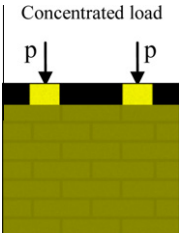
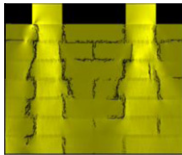
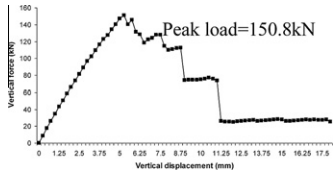
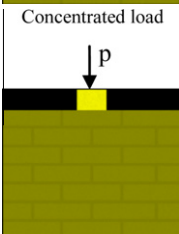
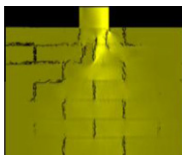
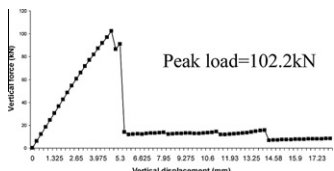
where σ_1 and σ_3 are the major and minor principal stresses, respectively; f_{c0} is the uniaxial compressive strength; and ϕ is the internal friction angle of the mesoscopic element. This kind of damage is called compressive/shear damage because the damage occurs when the stress conditions of an element meet the Mohr-Coulomb criterion. According to the Mohr-Coulomb criterion, when the element is under uniaxial compression, the expression for the damage variable D can be described as (Zhu and Tang, 2002; Zhu et al., 2004):

$$D = \begin{cases} 0 & \varepsilon < \varepsilon_{c0} \\ 1 - \frac{\lambda \varepsilon_{c0}}{\varepsilon} & \varepsilon \geq \varepsilon_{c0} \end{cases} \quad (9)$$

where λ is the residual strength coefficient and equal to f_{cr}/f_{c0} or f_{tr}/f_{t0} when the element is under uniaxial compression or tension. Previous work with the code (Zhu et al., 2004) has shown that, provided λ is in the range $0 < \lambda \leq 0.1$, the effect of the constitutive parameters on failure evolution is minor.

Table 3

Numerically simulated results compared with laboratory test results.

Batch	Model setup and loading arrangement	Numerically simulated failure results	Numerical simulated force-displacement curve and peak load (kN)	Ultimate experimental test load (kN) (Riddington and Naom, 1994)
1	Distributed load 		 Peak load=485.4kN	480
2	Concentrated load 		 Peak load=150.8kN	149
3	Concentrated load 		 Peak load=102.2kN	98.4

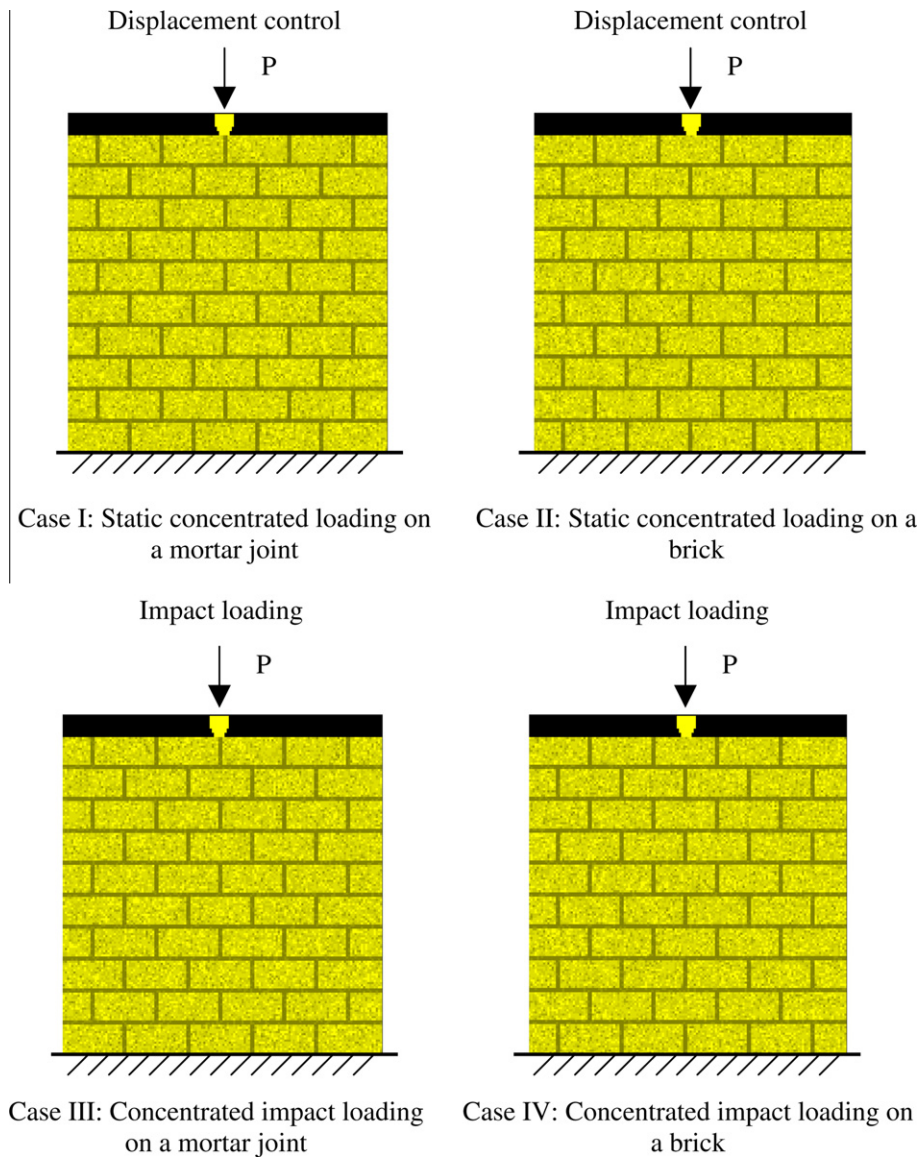


Fig. 1. Numerical model setups of four kinds of masonry tests: Case I. Static concentrated loading on a mortar joint; Case II. Static concentrated loading on a brick; Case III. Concentrated impact loading on a mortar joint; Case IV. Concentrated impact loading on a brick.

When an element is in a multi-axial stress state and its stress exceeds the Mohr-Coulomb criterion, damage occurs and the effect of the other principal stresses should be considered. When the Mohr-Coulomb criterion is met, the maximum principal strain (maximum compressive principal strain) ε_{c0} is calculated at the peak value of maximum principal stress (maximum compressive principal stress) according to (Zhu and Tang, 2002; Zhu et al., 2005):

$$\varepsilon_{c0} = \frac{1}{E_0} \left[f_{c0} + \frac{1 + \sin \varphi}{1 - \sin \varphi} \sigma_3 - \mu(\sigma_1 + \sigma_2) \right] \quad (10)$$

For these conditions, the shear damage evolution is related only to the maximum compressive principal strain, ε_1 , which can be substituted for the uniaxial compressive strain in Eq. (9). Thus the damage variable for multiaxial shear damage becomes (Zhu and Tang, 2002; Zhu et al., 2004):

$$D = \begin{cases} 0 & \varepsilon_1 < \varepsilon_{c0} \\ 1 - \frac{\lambda \varepsilon_{c0}}{\varepsilon_1} & \varepsilon_1 \geq \varepsilon_{c0} \end{cases} \quad (11)$$

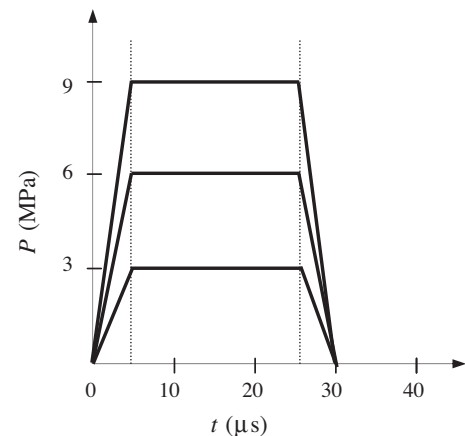


Fig. 2. Applied dynamic impact compressive stress waves with P_{\max} values of 3, 6 and 9 MPa.

In RFPA^{2D}, the specified displacement (or load) is applied to the specimen incrementally. If some elements are damaged in a particular step, their reduced elastic modulus at each stress or strain level is calculated using the above damage variable D as well as Eq. (2). Then the calculation is restarted under the current boundary and loading conditions to redistribute the stresses in the specimen until no new damage occurs. Finally the external load (or displacement) is increased and is used as input for the next step of the analysis. Therefore, the progressive failure process of a

brittle material subjected to gradually increasing static loading can be simulated. A user-friendly pre- and post-processor is integrated in RFPA^{2D} to prepare the input data and display the numerical results.

In addition, an Acoustic Emission (AE) technique is used to monitor the cracking processes taking place in some portions of the masonry structure (Carpinteri et al., 2004). In RFPA^{2D}, the failure (or damage) of every element is assumed to be the source of an acoustic event because the failed element must release its elastic

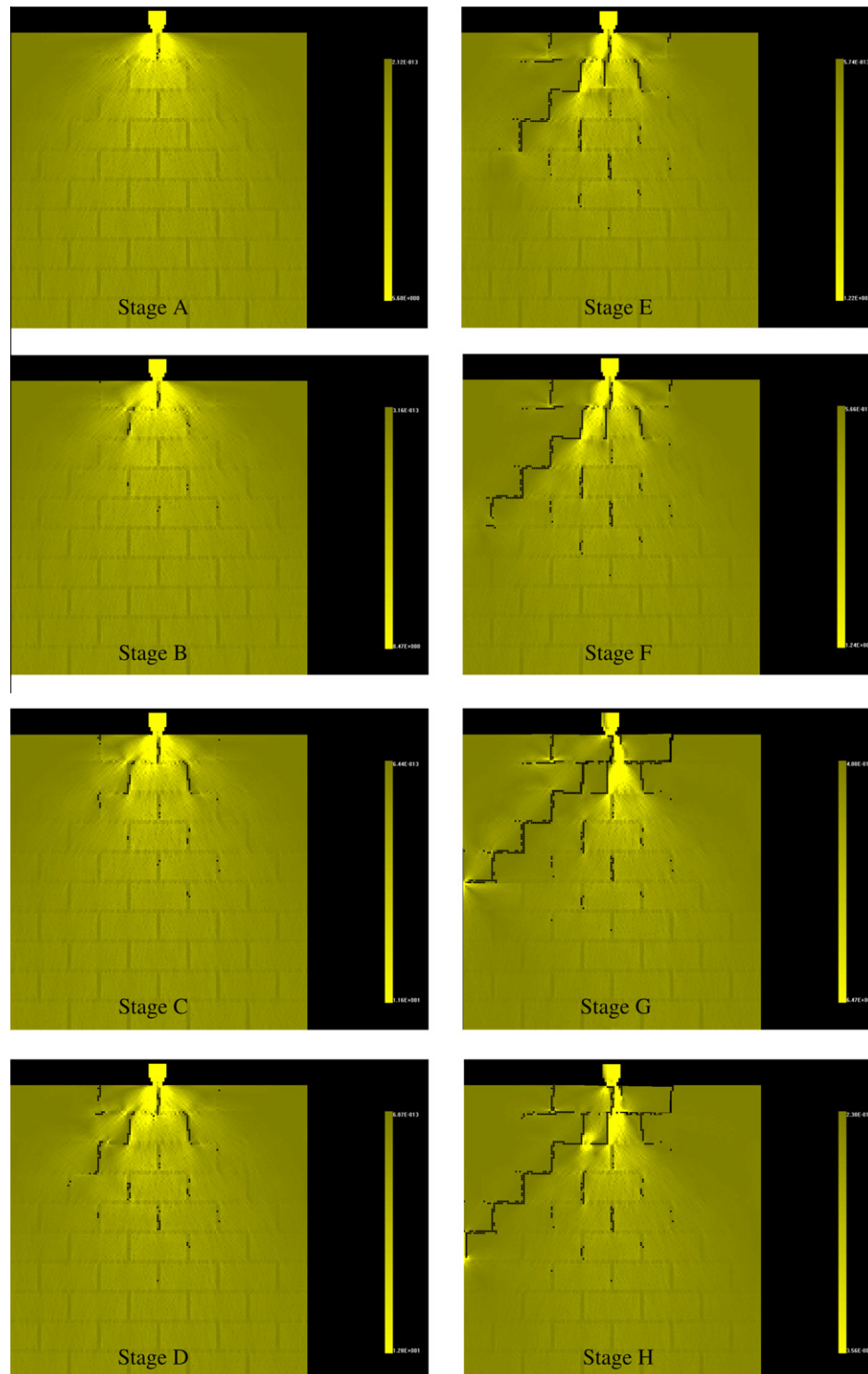


Fig. 3. Numerically simulated failure process of masonry due to concentrated load on a mortar joint (Shear stress distribution).

energy stored during the deformation. Therefore, by recording the number of damaged elements and the associated amount of energy release, RFPA^{2D} is capable of simulating AE activities, including the

AE event rate, magnitude and location. According to Tang and Kaiser (1998) the accumulative damage, D can be calculated by the following Eq. (6):

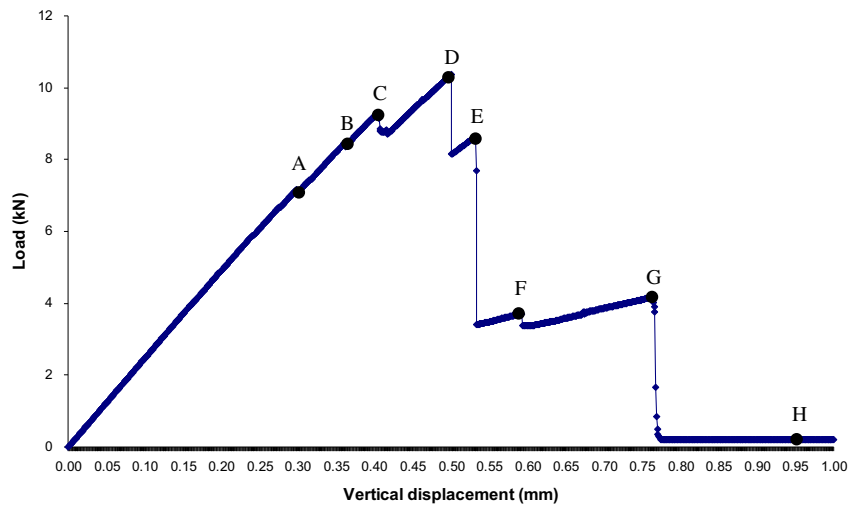


Fig. 4. Load-displacement behaviour of masonry due to concentrated load on a mortar joint.

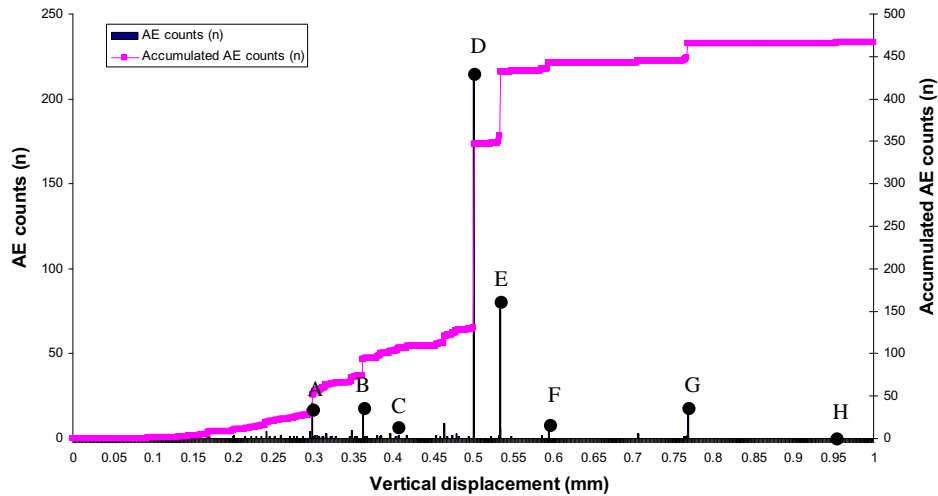


Fig. 5. AE counts and accumulated AE counts versus vertical displacement during the masonry failure process resulting from a concentrated load on a mortar joint.

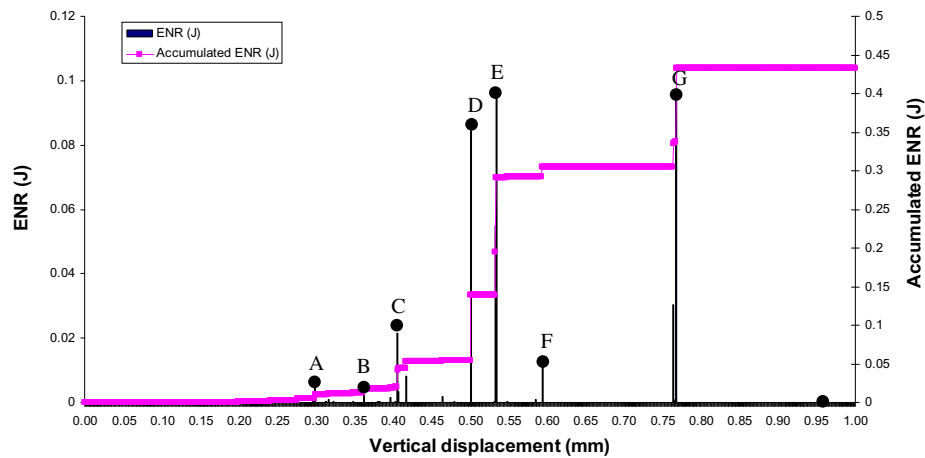


Fig. 6. Elastic energy release (ENR) and accumulated ENR versus vertical displacement during the masonry failure process because of the concentrated load on a mortar joint.

$$D = \frac{1}{N} \sum_{i=1}^s n_i$$

(12)

where s is the number of calculation steps, n_i is the damaged elements in the i th step and N is the total number of elements in the

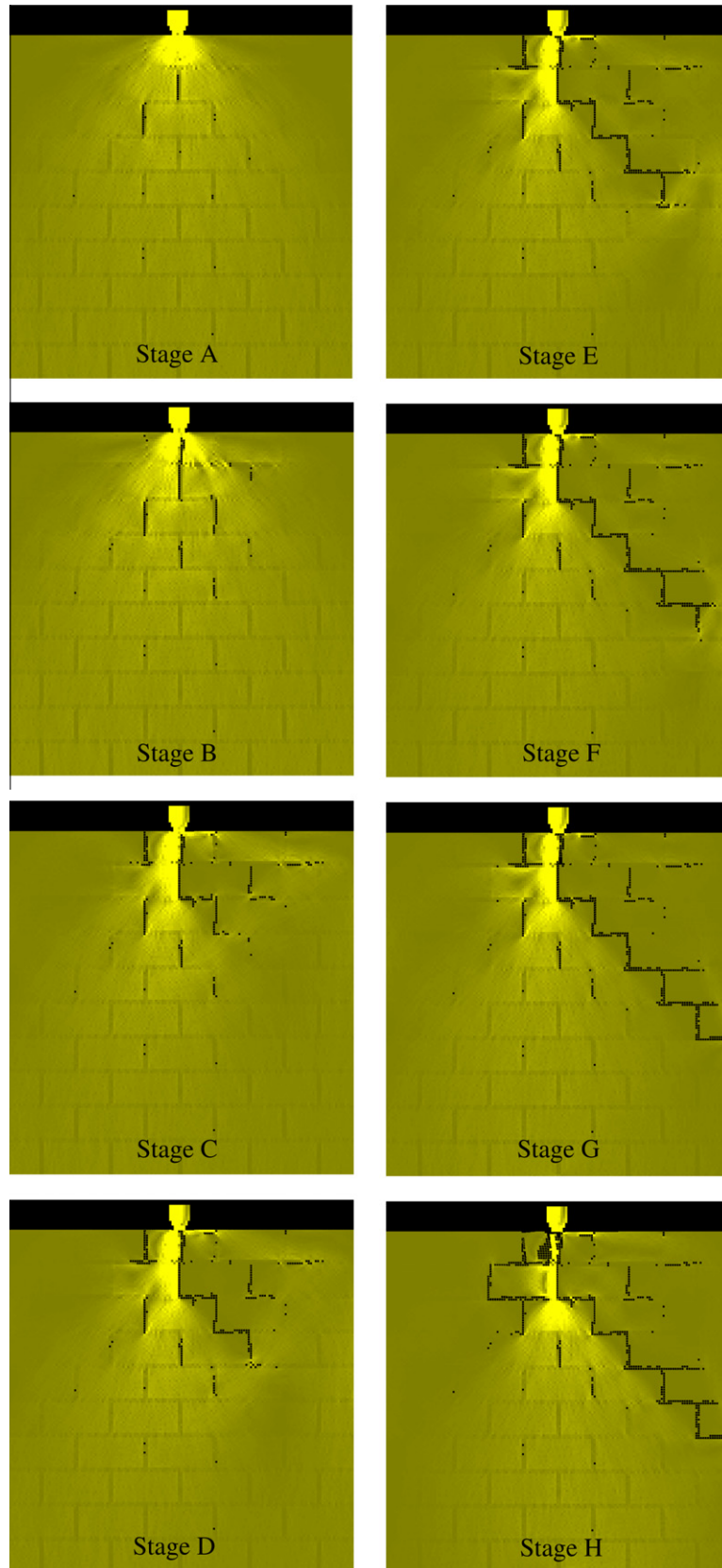


Fig. 7. Numerically simulated failure process of masonry due to a concentrated load on a brick (shear stress distribution).

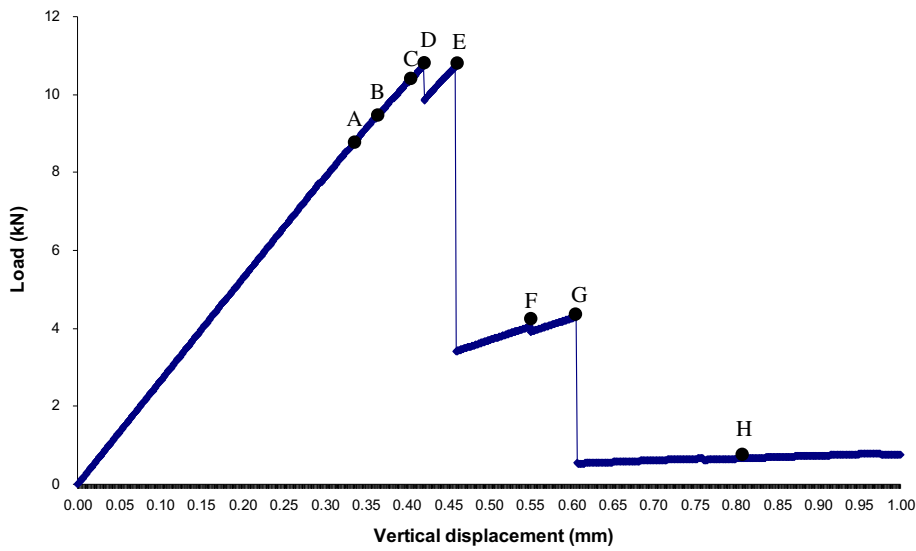


Fig. 8. Load-displacement behaviour of masonry due to concentrated load on a brick.

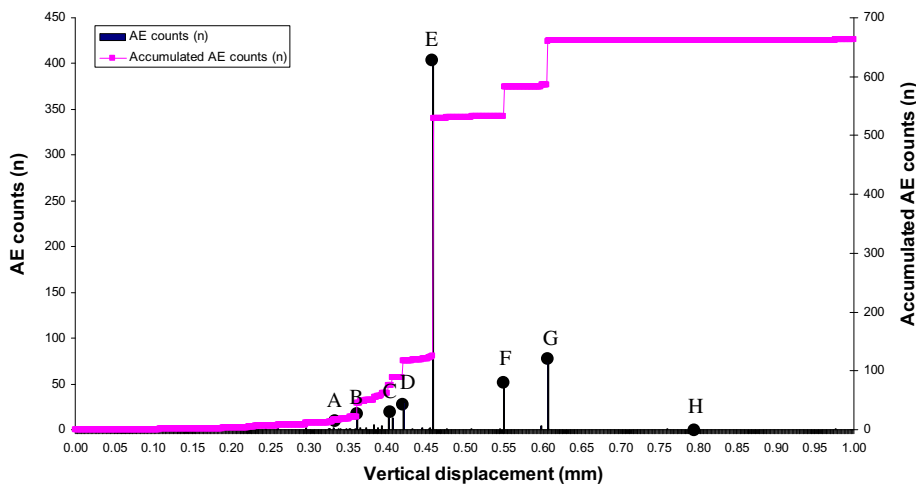


Fig. 9. AE counts and accumulated AE counts versus vertical displacement during the process of masonry failure due to concentrated load on a mortar joint.

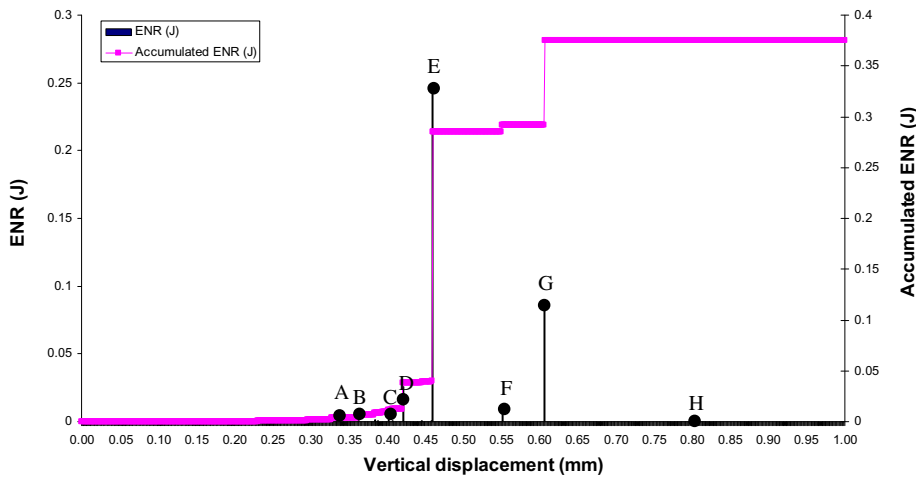


Fig. 10. Elastic energy release (ENR) and accumulated ENR versus vertical displacement during the process of masonry failure resulting from a concentrated load on a brick.

model. In addition, when the element fails, the energy released is calculated by Eq. (7) (Tang et al., 2007):

$$W_i = \frac{1}{2E}(\sigma_1^2 + \sigma_3^2 - 2\nu\sigma_1\sigma_3)V, \quad (13)$$

where i is the element number, W_i is the released elastic strain energy, E is the elastic modulus, σ_1 and σ_3 is the major and minor principle stress, respectively, ν is the Poisson ratio, and V is the element volume (Tang et al., 2007). AE activity indicates the extent of local damage in rock, which is directly associated with the evolution and propagation of fractures. By recording the counts of all failed elements and released energies when failure occurs, the AE phenomena associated with the progressive failure process can be simulated.

2.2. Strain-rate-dependent damage threshold

The above-mentioned constitutive law based on elastic damage mechanics is independent of the strain rate. Based on a variety of experimental results for granite, Zhao (2000) proposed that the Mohr-Coulomb criterion is also applicable to dynamic loading conditions if the increase in cohesion with the strain rate is taken into account. The relation between dynamic uniaxial compressive strength and the loading rate can be described with a semi-log formula as follows (Zhao, 2000):

$$f_{cd} = A \log(\dot{f}_{cd}/\dot{f}_{c0}) + f_{c0} \quad (14)$$

where f_{cd} is the dynamic uniaxial compressive strength (MPa); \dot{f}_{cd} is the dynamic loading rate (MPa/s); \dot{f}_{c0} is the quasi-brittle loading rate (approximately 5×10^{-2} MPa/s); and f_{c0} is the uniaxial compressive strength at the quasi-static loading rate. The parameter A reflects the effect of strain rate on the dynamic strength. In this investigation, the values of A for different materials are obtained based on the assumption that A increases linearly with the uniaxial compressive strength. In this respect, the strain rate effect on strength can be indirectly taken into account in the previously described constitutive law for the mesoscopic elements (Zhu and Tang, 2002; Chau et al., 2004). It is note that, according to Zhao (2000), this strain-rate-dependent damage law is applicable for brittle rock. Considering the present research also focusing on the brittle brick masonry, whose brittle properties can be verified by the experimental and numerical results in Table 3, accordingly, it is reasonable to assume the damage law (Zhao, 2000) is also applicable to brittle brick masonry. Nevertheless, the further work will

be carried out to evaluate this damage law (Zhao, 2000) to brittle brick masonry, based on experimental tests.

In addition, mesh sensitivity is an important issue that can influence the numerical results. Softening laws always induce mesh dependency upon mesh refinement as a result of the loss of well-posedness of the equilibrium boundary value problem. Zhu et al. (2004) has discussed the effect of element size on the numerically simulated results, by fixing the element size for the static problem. Furthermore, rate dependent laws adopted in the present model can actually be beneficial since rate dependency can contribute to the decrease of the mesh dependency issue.

2.3. Finite element implementation

As described above, the masonry specimen is discretised into rectangular four-noded elements (90,000 elements were typically used). The equilibrium equations governing the linear dynamic response of a system of finite elements can be expressed in the following form (Zhu and Tang, 2006):

$$M\ddot{U} + C\dot{U} + KU = R, \quad (15)$$

where M , C and K are the mass, damping, and stiffness matrices; R is the vector of externally applied loads or unbalanced forces; and U , \dot{U} and \ddot{U} are the nodal displacement, velocity, and acceleration vectors. A lumped mass analysis is assumed, where the structure mass is the sum of the individual element mass matrices plus additional concentrated masses that are specified at selected degrees of freedom. It is noted that Rayleigh damping is assumed, i.e. $C = \alpha M + \beta K$ (Clough and Bathe 1972). Here α and β are damping factors. A direct step-by-step integration procedure is found suitable for solving the problem in which a body is subjected to a short duration impulse loading (Tedesco et al. 1991). Wilson θ method of implicit time integration with a consistent mass formulation is employed and for unconditionally stability we need to use $\theta \geq 1.37$, and usually we employ $\theta = 1.4$ in our numerical analysis (Zhu and Tang, 2006).

For this kind of dynamic response problem, the maximum time step is related to the wave speed in the material and the size of finite element. The maximum time step is selected such that the stress wave cannot propagate further than the distance between the element integration points within the time increment.

The above constitutive law for studying the failure of rock specimens subjected to a variety of static stress conditions has been validated and published elsewhere (Zhu et al., 2005; Wang et al.,

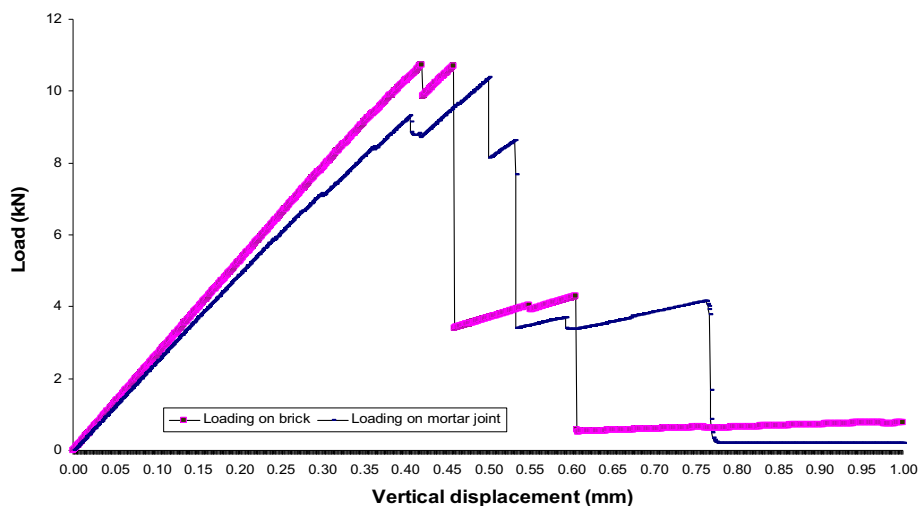


Fig. 11. Comparison of load-displacement behaviour of masonry due to a concentrated load on a mortar joint and brick.

2006; Zhu and Tang, 2006; Wang et al., 2011). For the dynamic analysis part of the RFP, the wave propagation in a one-dimensional prismatic bar subject to an axial loading was calculated

and compared to an available analytical solution in a previous study (Chau et al., 2004). In this paper, further validation of the failure process analysis is provided.

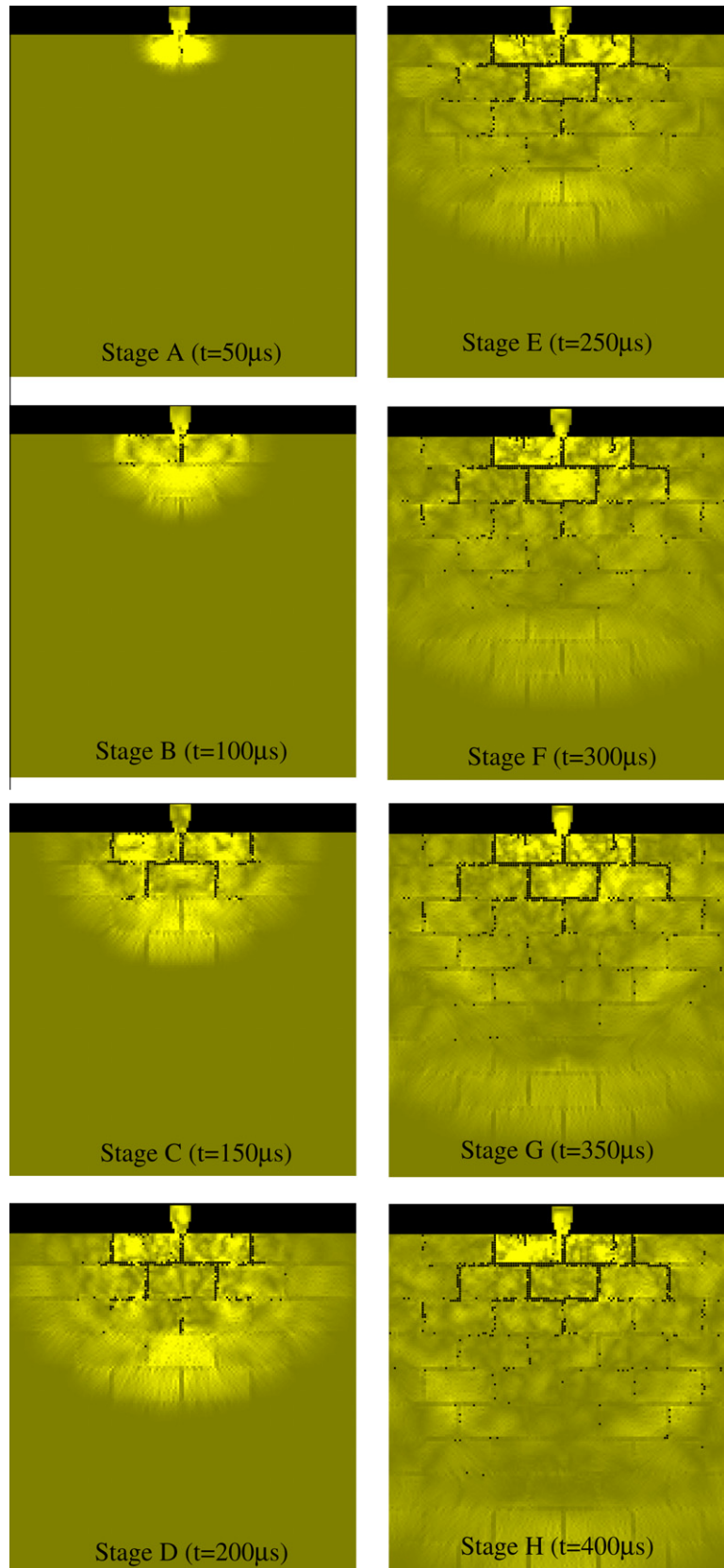


Fig. 12. Numerical simulated failure process of a masonry structure resulting from a concentrated impact load on a mortar joint ($P_{\max} = 6 \text{ MPa}$) (Shear stress distribution).

2.4. Static validation of numerical model

In order to validate the RFPA code to simulate the masonry structure, the experimental results (Riddington and Naom, 1994) obtained from wallettes of batches 1, 2 and 3 in Table 3 were used. As the wallettes tested were 325.0 mm wide, 240.0 mm high and 49.0 mm thick (Riddington and Naom, 1994), the model is discretised into $325 \times 240 = 78,000$ elements and the problem is simplified to a plane stress condition. Each complete brick comprises $105 \times 30 = 3150$ elements to represent the size of brick (105.0×30.0 mm). The nominal tested joint thickness of 5.0 mm was represented by five elements in the numerical model. For this numerical model, the brick masonry is assumed to be a three-phase composite composed of brick, mortar joints and their interfaces. The basic properties of the brick, mortar and the brick-mortar interface are presented in Table 1 (Riddington and Naom, 1994). The strength and elastic modulus of the indenters in the current models are given sufficiently high values such that they do not deform plastically during the masonry failure process – see Table 2.

It should be noted that, due to the heterogeneity of the material, it is difficult to set up the exact same wall for every test – even in

laboratory tests under controlled conditions. Therefore, in the current numerical model, the homogeneity index m is fixed to generate almost the same wall in each case. The effect of varying the parameter m for the masonry wall will be discussed in a separate paper.

At the initial condition, the elements are elastic and their stresses can be calculated using direct step-by-step explicit integration. During each time step, the principal stresses from the previous time step are subtracted from the current principal stresses and divided by the time step to calculate the element stress rates. These stress rates are then converted into strain rates by dividing by the Young's modulus. Similarly, when the current minor principal stress and corresponding stress rate are both negative, the increased strength of the element due to the increase in absolute value of the stress rate can also be obtained. When the stress rate effect is considered and the stresses (or strains) for an element meet the maximum tensile strain criterion or Mohr-Coulomb criterion, it undergoes damage according to the constitutive law given previously. The stress is then re-analysed iteratively using the current boundary conditions to reflect the stress redistribution at this time step. The program does not proceed to the next time step until no new damaged elements are found during the iteration in a

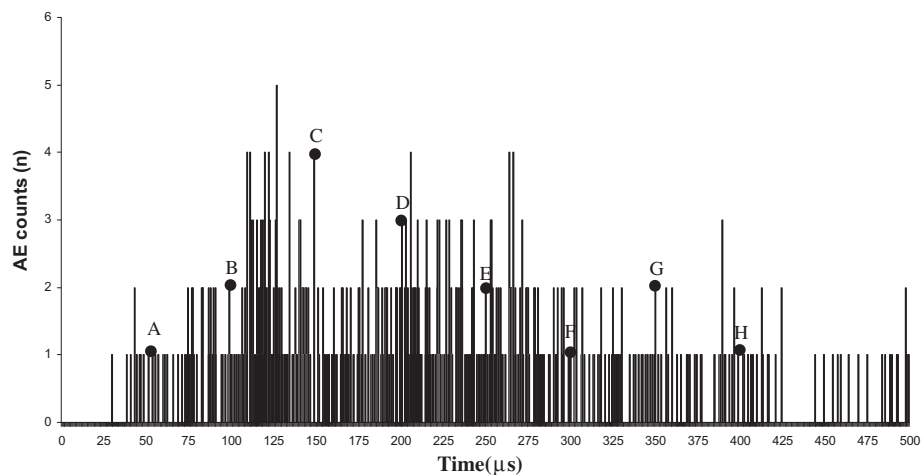


Fig. 13. Numerical simulated AE counts versus time for the case of a concentrated impact load on a mortar joint.

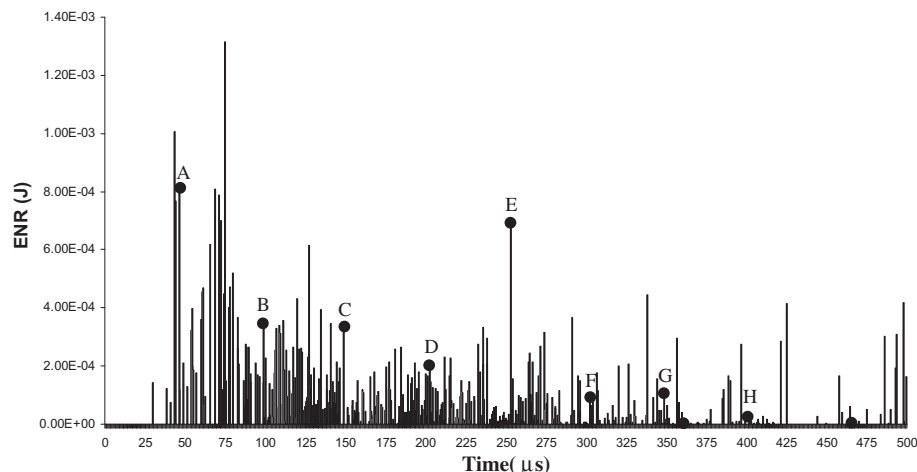


Fig. 14. Numerical simulated elastic energy release (ENR) versus time for the case of a concentrated impact load on a mortar joint.

current time step. More descriptions about the numerical simulations under static and dynamic loading have been presented in previous publications (Ross et al., 1995; Wang et al., 2011).

The numerically simulated failure modes and peak loads for each wallette batch compared to the averaged experimental results are shown in Table 3. The numerically simulated results

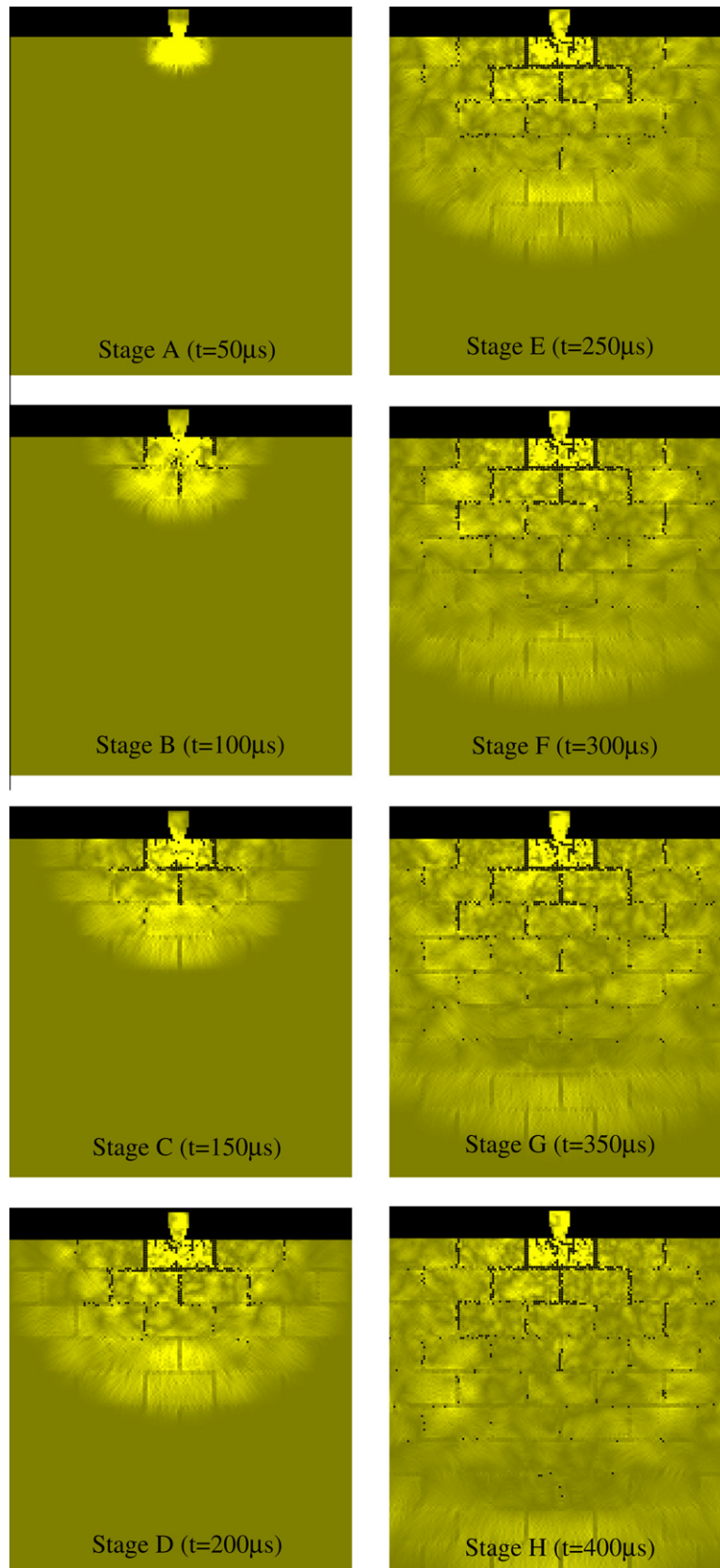


Fig. 15. Numerical simulated failure process of masonry structure resulting from a concentrated impact load on a brick ($P_{\max} = 6 \text{ MPa}$) (Shear stress distribution).

show very good agreement with the experimental results for batches 1, 2 and 3. For example, from numerically simulated three force-displace curves, the peak load obtained is 485.4,

150.8 and 102.2 kN, respectively, and the experimental ultimate load is 480, 149, 98.4 kN, respectively. Considering the complexity of the problem and the variability of the materials, this is not

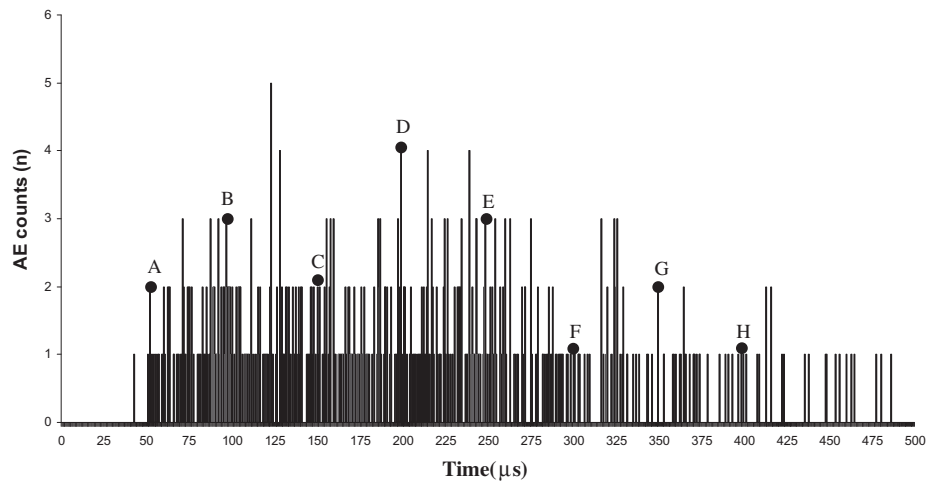


Fig. 16. Numerical simulated AE counts versus time for the case of a concentrated impact load on a brick.

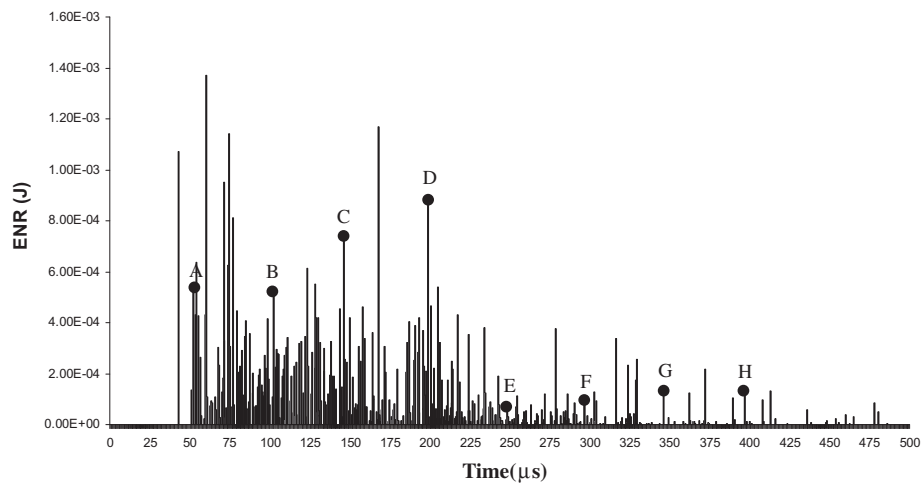


Fig. 17. Numerical simulated elastic energy release (ENR) versus time for the case of a concentrated impact load on a brick.

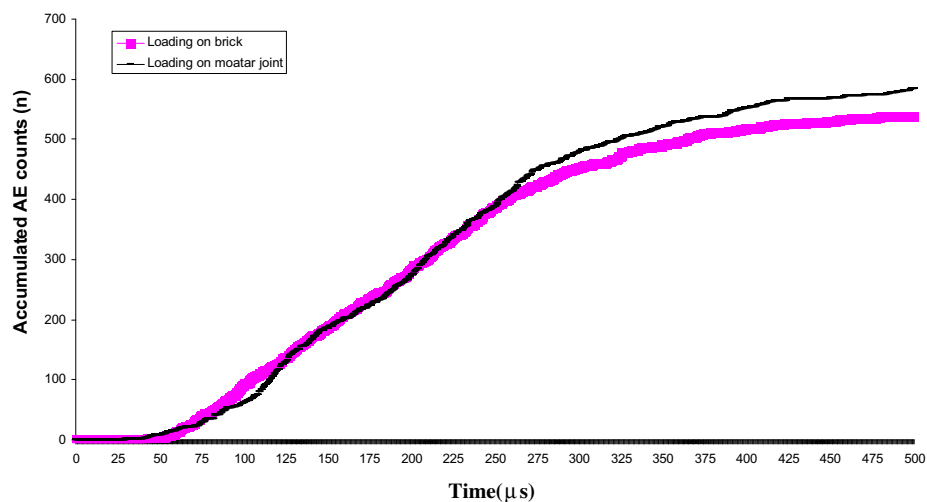


Fig. 18. Comparison of accumulated AE counts versus time for the cases of concentrated impact load on a mortar joint and a brick.

considered to be an unreasonable level of accuracy (Riddington and Naom, 1994).

In addition, numerically simulated results show that the failure modes for the batches 1, 2 and 3 are different. For instance, for batch 1, the cracks initiated from the bottom bricks and mortar joints and propagated upwards. As a comparison, for batch 2 and 3, due the concentrated loads, the cracks initiated underneath the indenter(s) and then propagated downwards. Furthermore, the propagation of cracks from indenter(s) are unsymmetrical. The failure characterises of cracks initiation and propagation due to concentrated loads will be discussed in the following section.

3. Numerical simulation of the failure process of unreinforced masonry walls due to concentrated static and dynamic loading

3.1. Model setup

In these numerical simulations the problem is simplified to a plane stress condition, as shown in Fig. 1. In total, four cases are considered. Case I represents a static concentrated loading applied directly to the mortar joint; Case II represents a static concentrated loading applied on the brick at mid-length; Case III represents a concentrated impact load on a mortar joint; and Case IV represents a concentrated impact load on a brick. For the static cases, a displacement increment (0.005 mm/step) is applied to the indenters. For the dynamic cases, three kinds of compressive stress wave are applied, as shown in Fig. 2. The basic properties of the brick, mortar and the brick-mortar interface are adopted with the same in Table 1 (Riddington and Naom, 1994). The strength and elastic modulus of the indenters in the current models are also shown in Table 2.

In the simulations, the model is discretised into $320 \times 345 = 110,400$ elements that are 320 mm wide and 345 mm high. The size of the bricks is 60 mm wide and 30 mm high. Each complete brick comprises $60 \times 30 = 1800$ elements, while the mortar joint thickness is 5 mm with 5 elements.

3.2. Numerically simulated results for the failure process of masonry walls subjected to static concentrated loads

In this section, two kinds of numerical simulations are carried out to study the failure pattern of masonry walls. Case I represents a sta-

tic concentrated loading applied on the mortar joint, and Case II represents a static concentrated loading applied on the brick (Fig. 1).

3.2.1. Case I of static concentrated load on the mortar joint

Fig. 3 shows the numerically simulated failure process of brick masonry for the case of a static concentrated load on a mortar joint. Figs. 4–6 show, respectively, the corresponding load-displacement behaviour, AE count-displacement plot and elastic energy release (ENR)-displacement plot. From Fig. 3, it is clear that the stress concentrates below the indenter and, then, because the strength of mortar is much lower than that of brick, the initial cracking occurs along the vertical mortar joint (Stage A). As the vertical loads increase, more cracks occur in the vertical mortar joints in the next course down from the top, and the previous cracks develop downwards along the vertical mortar joints (Stages B and C). During these stages, the cracking propagates as the load increases, which indicates that the crack propagation is stable. It can be verified from Fig. 4 that the load-displacement plot is almost linearly increasing from Point A to Point C. After this, some cracks occur in the horizontal mortar joints, as shown in the first and second horizontal mortar joints (Fig. 3 Stage D). Furthermore, both the vertical and horizontal cracks propagate until they coalesce and form a stepped crack (Fig. 3 Stage E). During some stages (Stages D and E), the crack propagation is accompanied by a decrease in the applied load, as shown at Points D and E in Fig. 4. This indicates that the crack propagation is unstable. Correspondingly, from Figs. 5 and 6, both the AE counts and the elastic energy release (ENR) increase significantly at points D and E.

It is noted that the initial vertical crack below the indenter starts to propagate and pass through the brick in the second course (Stages E and F). As the vertical loads increase, most horizontal and vertical cracks propagate along the mortar joints, and no more cracks traverse the brick (Stages G and H). Finally, cracks reach a depth of approximately 60% of the wall height. It is interesting to find that the ultimate stepped cracks only propagate to the left of the wall, and no symmetrical stepped cracks occur in the right section. This is because the properties of the brick and mortar joints are different materials which are shown in Table 1. Moreover, according to Weibull distribution (Eq. (1)), the mechanical properties of each brick and mortar joints such as the elastic modulus, the strength and Poisson's ratio are not the same. Therefore, the masonry wall material is heterogeneous, and the stress distribution due to the concentrated load will not be homogeneous and symmetric. As a result, the cracking pattern is also not symmetrical.

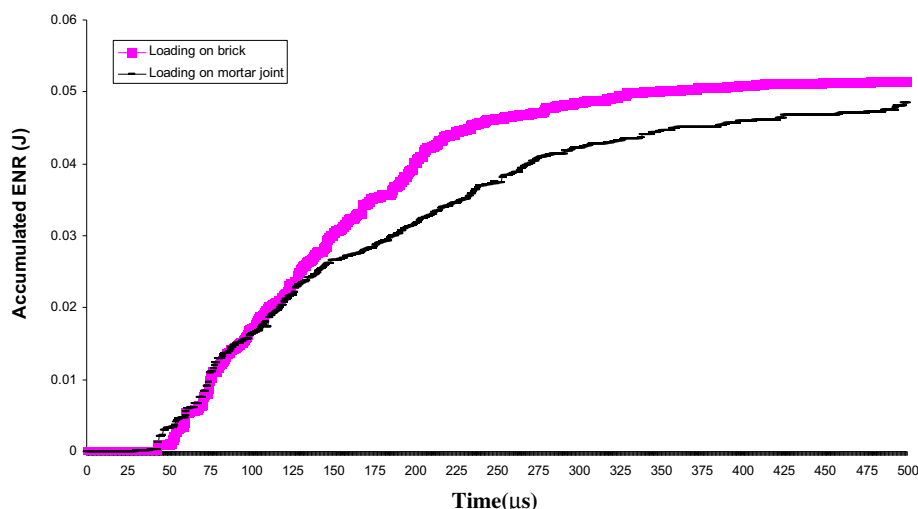


Fig. 19. Comparison of accumulated elastic energy release (ENR) versus time for the cases of a concentrated impact load on a mortar joint and a brick.

3.2.2. Case II of a static concentrated load on a brick

Fig. 7 shows the numerically simulated failure process of brick masonry for the case of a static concentrated load on a brick. Figs. 8–10 show, respectively, the corresponding load-displacement behaviour, AE count-displacement plot and elastic energy release-displacement plot. Comparing Fig. 3 with Fig. 7, stress concentrates below the indenters in stage A. However, the initial vertical cracks occur in mortar joints in the second and the third courses, not the first course mortar joint as in Fig. 3. This is because the strength of the brick material is much higher than that of the mortar joints. When the concentrated load is applied to the brick, the stress from the indenter is transferred downwards before brick failure occurs, which results in crack initiation and propagation in the second course. As the vertical loads increase, more cracks occur in the subsequent vertical mortar joints. In the meantime, cracks

initiate and propagate in the brick directly below the indenter in Stages B and C of Fig. 7.

Comparing Fig. 4 with Fig. 8, the crack propagation is stable from Stages A to C. It can also be verified from Fig. 8 that the load-displacement plot is almost linearly increasing from Point A to Point C. However, in Stages D, E and G, crack propagation is unstable. Correspondingly, from Figs. 9 and 10, both the AE counts and elastic energy release increase significantly at Points D, E and G. As before, the ultimate stepped cracks are also not symmetrical due to the heterogeneity of the masonry wall, but this time the stepped cracks form in the right half instead of the left half (Fig. 3). Comparing the two cases of concentrated loading on a mortar joint and a brick, a higher load is required to reach brick failure than mortar joint failure in the initial stage because the strength of brick is higher than that of mortar. This is why the

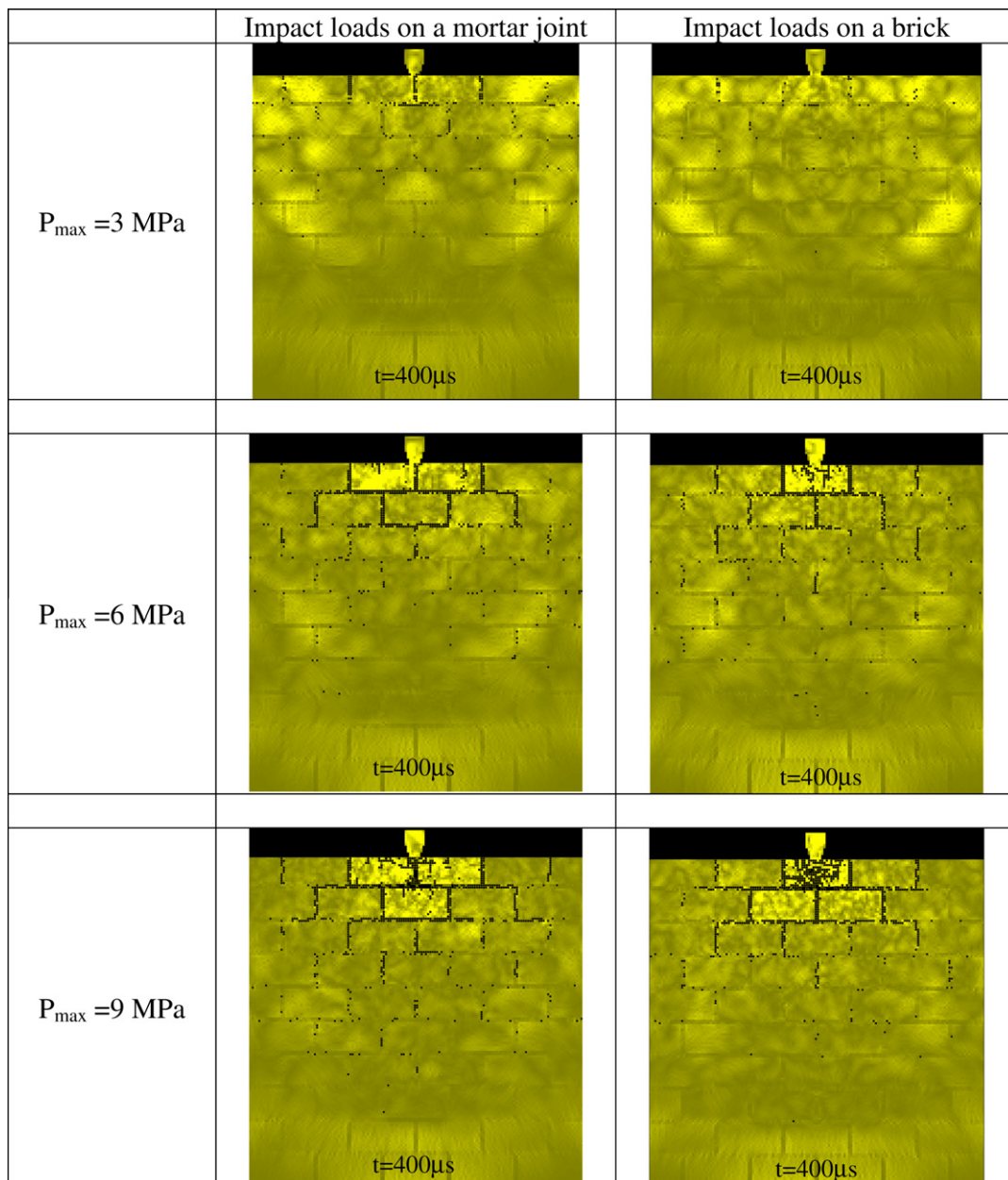


Fig. 20. Comparison of failure modes for the cases of concentrated loads on a mortar joint and a brick with P_{\max} values of 3, 6 and 9 MPa.

load-displacement plot for the brick loading lies above that for the mortar joint loading in Fig. 11.

3.3. Numerically simulated results for the failure process of masonry walls subjected to dynamic (impact) concentrated loads

In this section, two kinds of numerical simulations are performed to study the masonry wall failure patterns. Case III represents dynamic concentrated loading on a mortar joint, while Case IV represents dynamic concentrated loading on a brick (Fig. 1). The maximum stress (P_{\max}) of the compressive stress waves of the two cases is 6 MPa, as shown in Fig. 2. Finally, the effect of varying the magnitude of the compressive stress waves (P_{\max}) on the failure pattern is discussed.

3.3.1. Case III of dynamic concentrated load on a mortar joint

Fig. 12 shows the numerically simulated failure process of a masonry wall for the case of a dynamic concentrated load on a mortar joint. Figs. 13 and 14 show, respectively, plots of the corresponding AE counts and elastic energy release (ENR) over time. The durations for the indenter compressive stresses are fixed to be 500 μs . During the first stage of loading (Stage A, $t = 50 \mu\text{s}$),

the stress fields induced by the indenter are similar to those induced by the case of static loading in Fig. 3 (Stage A). The zone immediately under the indenter is highly stressed, and a few cracks are initiated and develop in the vertical and horizontal mortar joints (Stage B, $t = 100 \mu\text{s}$). In the meantime, vertical tensile cracks occur on the upper face of the bricks that lie either side of the indenter. As the compressive stress waves from the impact propagate during Stages C to H in Fig. 12, more cracks initiate and propagate in the vertical and horizontal mortar joints. During this period, vertical tensile cracks develop downwards but do not traverse the bricks.

Comparing the final stage H in Fig. 12 with the final stage H in Fig. 3, it is clear that the ultimate crack pattern for the dynamic case is almost symmetric. This is because the compressive wave propagates through the wall in a symmetric manner. However, because of the heterogeneity of the brick and mortar that has been noted previously, the ultimate crack pattern of the masonry wall is also not totally symmetric. Due to the damping effect of the masonry wall material, the gradual attenuation of the compressive stress waves results in less cracking at points away from the indenter. Figs. 13 and 14 indicate that both the AE counts and ENR are also reduced.

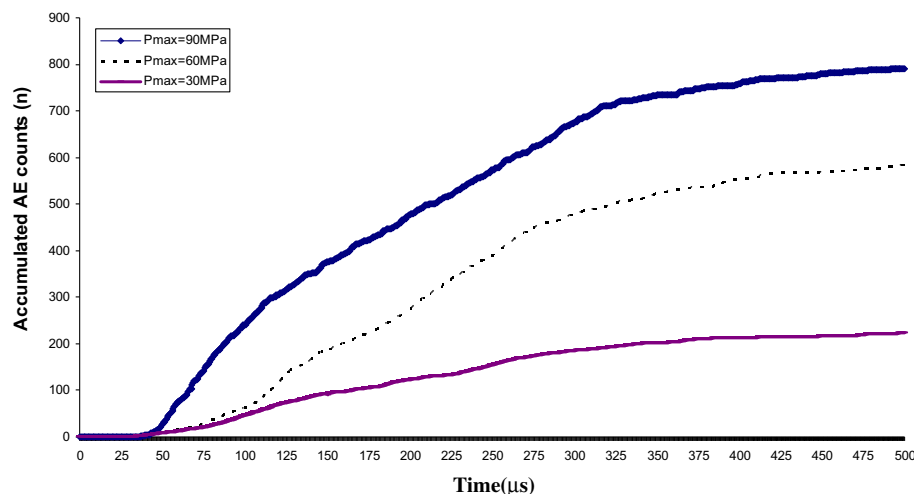


Fig. 21. Comparison of accumulated AE counts versus time for the cases of concentrated load on a brick with P_{\max} values of 3, 6 and 9 MPa.

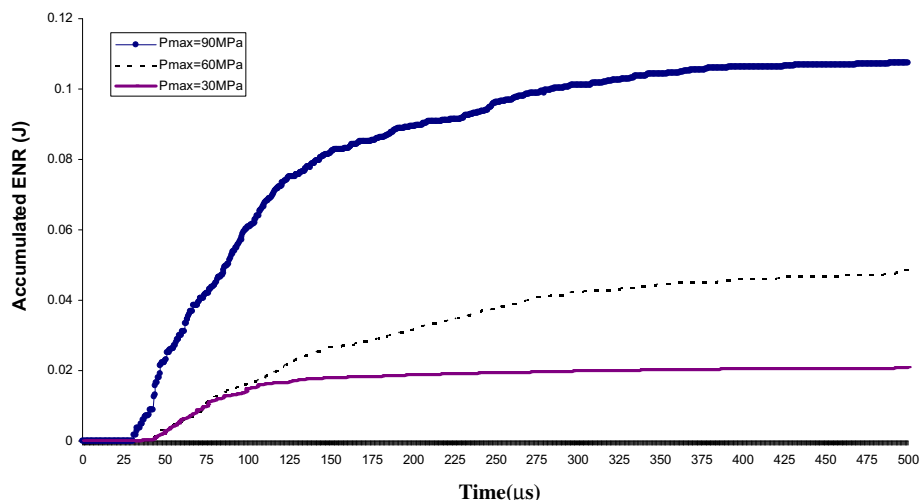


Fig. 22. Comparison of accumulated ENR versus time for the cases of concentrated load on a brick with P_{\max} values of 3, 6 and 9 MPa.

3.3.2. Case IV of dynamic concentrated load on a brick

Fig. 15 shows the numerically simulated masonry wall failure process for the case of dynamic concentrated load on a brick. Figs. 16 and 17 show, respectively, the corresponding AE counts and elastic energy release plots versus time. The duration of the indenter compressive stresses are again fixed to be 500 μ s. During the first stage of loading (Stage A, $t = 50 \mu$ s), the stress fields induced by the indenter are similar to those induced by the case of static loading in Fig. 7 (Stage A). However, comparing stages B and C in Fig. 15 with those in Fig. 7, several small vertical tensile cracks occur along the upper surface of the brick beneath the indenter, while only one such crack occurs in these stages for the static case in Fig. 7. Moreover, the final failure pattern for the brick beneath the indenter is also different. The brick splits into two parts via the single vertical crack in the case of static loading, while the brick is fragmented by many small cracks that coalesce under dynamic loading.

Comparing the final stage H in Fig. 12 with the final stage H in Fig. 15, the ultimate crack pattern for the dynamic case with a concentrated load on a brick is also symmetric. Furthermore, Figs. 16 and 17 show that both the AE counts and elastic energy release diminish along with the compressive waves that develop because of the damping of the masonry material. As a comparison, Figs. 18 and 19 show the AE counts and elastic energy release, respectively, for dynamic loading on a brick and dynamic loading on a mortar joint. Fig. 18 shows that the accumulated AE accounts for the brick loading are generally lower than those for the mortar joint loading, while Fig. 19 shows that the reverse is true for the elastic energy release. This is because the strength of the brick is greater than that of the mortar joint, and so more energy is required to cause the brick failure than mortar joint failure.

3.3.3. Effect of the amplitudes of incident pressure

Fig. 20 presents the effect of three kinds of compressive stress waves on the failure pattern for a concentrated impact load on the mortar joint and a brick. The maximum stress (P_{\max}) for the three kinds of compressive stress waves is 3, 6 and 9 MPa, respectively, as shown in Fig. 2. For the purposes of comparison, the different failure patterns at $t = 400 \mu$ s are provided. For the mortar joint loading case with $P_{\max} = 3$ MPa, Fig. 20 shows vertical and horizontal cracking in the mortar joints only in the first course of the masonry wall, and there is no cracking in the brick beneath the indenter. By comparison, when P_{\max} is 6 MPa, more vertical and horizontal cracks occur in the first and second course mortar joints, and some vertical cracks emerge from the top surface of the bricks near the indenter. Moreover, when P_{\max} is 9 MPa, the vertical and horizontal cracks occur in the mortar joints of the first three courses of bricks, and more small cracks in the bricks are concentrated below the indenter, in addition to the cracks in the mortar joint.

Similarly, for the case of impact loads on the brick, when P_{\max} is 3 MPa, very few cracks occur in the vertical mortar joints in the first course of masonry wall. As P_{\max} increases to 6 and 9 MPa, more cracks occur in the horizontal and vertical mortar joints and brick. Figs. 21 and 22 show accumulated AE counts and ENR versus time for the two cases of concentrated load on the brick with the P_{\max} values of 3, 6 and 9 MPa, respectively. It is clear that with the increase of P_{\max} , more AE counts and higher elastic energy releases are observed.

4. Conclusions

In this study, RPPA^{2D} code has been applied to simulate static and dynamic failure processes of unreinforced in-plane masonry walls. In order to validate the RPPA^{2D} code to simulate the masonry

structure, the experimental results (Riddington and Naom, 1994) were used. The numerically simulated results show very good agreement with the experimental results. Although the reality is often much more complex than the applied numerical models, the study provides interesting indications for understanding of the failure mechanism of these structures. From the numerical simulations, the following conclusions are derived.

For the case of static concentrated load on a mortar joint and a brick, the numerical simulations show stable and unstable crack propagation, with the latter being identified by sudden load drop, high AE counts, and abrupt increases in the elastic energy release. In addition, the numerical results show the formation of nonsymmetrical stepped cracks at failure which is due to the heterogeneous nature of masonry. Because the strength of the brick is greater than that of a mortar joint, much more energy is required to cause brick failure than mortar joint failure for the same applied loads. Therefore, different concentrated loading locations lead to different initial failure patterns of the masonry walls.

For the case of a dynamic concentrated load on the mortar joint and brick, the numerical results show the failure process of masonry walls along with the compressive waves propagating downwards. In addition, due to the damping of the masonry material, the gradual attenuation of compressive waves results in fewer crack initiations as the distance from the indenter increases. Furthermore, numerical results show that the P_{\max} of the compressive stress waves plays an important role in the masonry wall failure pattern. With an increase in P_{\max} , more vertical and horizontal cracks occur in the mortar joints and more cracks appear in the bricks.

In contrast to the static load cases, the numerical results show that the ultimate crack pattern for the dynamic load case is almost symmetric. This is because the compressive waves propagate through the wall in a symmetric manner. However, because of the heterogeneity that is inherent in a masonry wall, the ultimate crack pattern is also not completely symmetric.

Suggestions for further work include validation of the proposed numerical model for the 2D failure under concentrated dynamic loading. Extension of the current 2D model to 3D configurations will be conducted to study the failure characteristics of masonry walls subject to out-of-plane impacts.

Acknowledgement

The work described in this paper was partially supported by an Australian Research Council grant DP0881238 and ARC Australian Laureate Fellowship grant FL0992039, for which the authors are very grateful.

References

- Ali, S., Page, A.W., 1998. Finite element model for masonry subjected to concentrated loads. *J. Struct. Div. ASCE* 114 (8), 1761–1784.
- Anthoine, A., 1997. Homogenisation of periodic masonry: plane stress, generalised plane strain or 3D modelling. *Commu. Numer. Methods Eng.* 13, 319–326.
- Bazant, Z.P., Gu, W.H., Faber, K.T., 1995. Softening reversal and other effects of a change in loading rate on fracture of concrete. *ACI Mater. J.* 92 (1), 3–9.
- Bigoni, D., Piccolroaz, A., 2004. Yield criteria for quasi-brittle and frictional materials. *Int. J. Solids Struct.* 4, 2855–2878.
- Burnett, S., Gilbert, M., Molyneux, T., Beattie, G., Hobbs, B., 2007. The performance of unreinforced masonry walls subjected to low-velocity impacts: Finite element analysis. *Int. J. Impact Eng.* 34 (8), 1433–1450.
- Carpinteri, A., Lacidogna, G., Pugno, N., 2004. A fractal approach for damage detection in concrete and masonry structures by the acoustic emission technique. *Acoust. Technol.* 38, 31–37.
- Cecchi, A., Rizzi, N.L., 2001. Heterogeneous elastic solids: a mixed homogenization-rigidification technique. *Int. J. Solids Struct.* 38, 29–36.
- Chau, K.T., Zhu, W.C., Tang, C.A., Wu, S.Z., 2004. Numerical simulations of failure of brittle solids under dynamic impact using a new computer program – DIFAR. *Key Eng. Mater.* 261, 239–244.

- Clough, R.W., Bathe, K.J., 1972. Finite element analysis of dynamic response. In: *Advances in Computational Methods in Structural Mechanics and Design*, University of Alabama, pp. 153–179.
- Dhanasekar, M., Kleeman, P.W., Page, A.W., 1985. Biaxial stress-strain relations for brick masonry. *J. Struct. Div. ASCE* 111 (5), 1085–1100.
- Essawy, A.S., Drysdale, R.G., Mirza, F.A., 1985. Non-linear macroscopic finite element model for masonry walls. In: *Proceedings of New Analysis Techniques for Structural Masonry*, ASCE Structures Congress'85, Chicago, Illinois.
- Gilbert, M., Hobbs, B., Molyneux, T.C.K., 2002. The performance of unreinforced masonry walls subjected to low-velocity impacts: experiments. *Int. J. Impact Eng.* 27 (3), 231–251.
- Guinea, G.V., Hussein, G., Elices, M., Planas, J., 2000. Micromechanical modelling of brick-masonry fracture. *Cement Concr. Res.* 30, 731–737.
- Ju, J.W., Moneriro, P.J.M., Rashed, A.I., 1989. Continuum damage of cement paste and mortar as affected by porosity and sand concentration. *J. Eng. Mech. ASCE* 115 (1), 105–130.
- Lofti, H.R., Shing, P.B., 1991. An appraisal of smeared crack models for masonry shear wall analysis. *Comput. Struct.* 41 (3), 413–425.
- Lourenco, P.B., 1996. *Computational Strategies for Masonry Structures*. Ph.D. Thesis. Delft University of Technology, Paises Baixos.
- Lourenco, P.B., Rots, J.G., 1997. Multisurface interface model for analysis of masonry structures. *J. Eng. Mech. Div. ASCE* 123 (7), 660–668.
- Lourenco, P.B., Rots, J.G., 2000. An anisotropic failure criterion for masonry suitable for numerical implementation. *TMS J.* 18 (1), 11–18.
- Mackerle, J., 2000. Finite element linear and nonlinear, static and dynamic analysis of structural elements – an addendum – a bibliography (1996–1999). *Eng. Comput.* 17 (3), 274–360.
- Mackerle, J., 2004. Finite element modelling and simulation of indentation testing: a bibliography (1990–2002). *Eng. Comput.* 21 (1), 23–52.
- Massart, T.J., Peerlings, R., Geers, M., 2004. Mesoscopic modelling of failure and damage induced anisotropy in brick masonry. *Eur. J. Mech. A. Solids* 23 (7), 19–35.
- Massart, T., Peerlings, R., Geers, M.D., Gottcheiner, S., 2005. Mesoscopic modelling of failure in brick masonry accounting for three-dimensional effects. *Eng. Fract. Mech.* 72, 1238–1253.
- Milani, G., Lourenco, P.B., Tralli, A., 2009. Homogenized rigid-plastic model for masonry walls subjected to impact. *Int. J. Solids Struct.* 46 (22–23), 4133–4149.
- Morris, J.P., Rubin, M.B., Block, G.I., Bonner, M.P., 2006. Simulations of fracture and fragmentation of geologic materials using combined FEM/DEM analysis. *Int. J. Impact Eng.* 33, 463–473.
- Page, A.W., 1983. The strength of brick masonry under biaxial tension-compression. *Int. J. Masonry Constr.* 3 (1), 26–31.
- Pande, G.N., Liang, J.X., Middleton, J., 1989. Equivalent elastic moduli for brick masonry. *Comput. Geotech.* 8, 243–265.
- Pina-Henriques, J., Lourenco, P.B., 2006. Masonry compression: a numerical investigation at the meso-level. *Eng. Comput.* 23 (3–4), 382–407.
- Riddington, J.R., Naom, N.F., 1994. Finite element prediction of masonry compressive strength. *Comput. Struct.* 52, 113–119.
- Rosenhaupt, S., Sokol, Y., 1965. Masonry walls on continuous beams. *J. Struct. Div. ASCE* 91 (1), 155–171.
- Ross, C.A., Thompson, P.Y., Tedesco, J.W., 1989. Split-Hopkinson pressure-bar tests on concrete and mortar in tension and compression. *ACI Mater. J.* 86 (5), 475–481.
- Ross, C.A., Tedesco, J.W., Kuennen, S.T., 1995. Effects of strain rate on concrete strength. *ACI Mater. J.* 92 (1), 37–47.
- Rots, J.G., 1991. Numerical simulation of cracking in structural masonry. *Heron* 36 (2), 49–63.
- Shieh-Beygi, B., Pietruszczak, S., 2008. Numerical analysis of structural masonry: mesoscale approach. *Comput. Struct.* 86, 1958–1973.
- Tang, C.A., 1997. Numerical simulation of rock failure and associated seismicity. *Int. J. Rock Mech. Min. Sci.* 34, 249–262.
- Tang, C.A., Kaiser, P.K., 1998. Numerical simulation of cumulative damage and seismic energy release during brittle rock failure-Part I: Fundamentals. *Int. J. Rock Mech. Min. Sci.* 35 (2), 113–121.
- Tang, C.A., Kou, S.Q., 1998. Crack propagation and coalescence in brittle materials under compression. *Eng. Fract. Mech.* 61 (3–4), 311–324.
- Tang, C.A., Liu, H., Lee, P.K.K., Tsui, Y., Tham, L.G., 2000. Numerical tests on micro-macro relationship of rock failure under uniaxial compression, part I: effect of heterogeneity. *Int. J. Rock Mech. Min. Sci.* 37, 555–569.
- Tang, C.A., Tham, L.G., Wang, S.H., Liu, H., Li, W.H., 2007. A numerical study of the influence of heterogeneity on the strength characterization of rock under uniaxial tension. *Mech. Mater.* 39, 326–339.
- Tedesco, J.W., Ross, C.A., Brunair, R.M., 1989. Numerical analysis of dynamic split cylinder tests. *Comput. Struct.* 32 (3), 609–624.
- Tedesco, J.W., Ross, C.A., McGill, P.B., O'Neil, B.P., 1991. Numerical analysis of high strain-rate concrete direct tension test. *Comput. Struct.* 40 (2), 313–327.
- Tedesco, J.W., Ross, C.A., Kuennen, S.T., 1993. Experimental and numerical analysis of high strain rate splitting tensile tests. *ACI Mater. J.* 90 (2), 162–169.
- Wang, S.H., Tang, C.A., Jia, P., 2006. Analysis of the shear failure process of masonry by means of a meso-scopic mechanical modeling approach. *Struct. Eng. Mech.* 24 (2), 181–194.
- Wang, S.Y., Sloan, S.W., Liu, H.Y., Tang, C.A., 2011. Numerical simulation of the rock fragmentation process induced by two drill bits subjected to static and dynamic loading. *Rock Mech. Rock Eng.* 44 (3), 317–332.
- Weibull, W., 1951. A statistical distribution function of wide applicability. *J. Appl. Mech.* 18, 293–297.
- Wood, R.H., 1952. *Studies in composite construction, part I. The composite action of brick panel walls supported on reinforced concrete beams*, Research Paper No. 13, National Building Studies, Building Research Station, Waterford, UK.
- Yon, J.H., Hawkins, N.M., Kobayashi, A.S., 1992. Strain-rate sensitivity of concrete mechanical properties. *ACI Mater. J.* 89 (2), 146–153.
- Zhao, J., 2000. Application of Mohr-Coulomb and Hoek-Brown strength criteria to the dynamic strength of brittle rock. *Int. J. Rock Mech. Min. Sci.* 37, 1115–1121.
- Zhu, W.C., Tang, C.A., 2002. Numerical simulation on shear fracture process of concrete using mesoscopic mechanical model. *Constr. Build. Mater.* 16 (8), 453–463.
- Zhu, W.C., Tang, C.A., 2006. Numerical simulation of Brazilian disk rock failure under static and dynamic loading. *Int. J. Rock Mech. Min. Sci.* 43, 236–252.
- Zhu, W.C., Teng, J.G., Tang, C.A., 2004. Mesomechanical model for concrete, part I: model development. *Mag. Concrete Res.* 56 (6), 313–330.
- Zhu, W.C., Tang, C.A., Wang, S.Y., 2005. Numerical study on the influence of mesomechanical properties on macroscopic failure of concrete. *Struct. Eng. Mech. Int. J.* 19 (5), 519–533.